



Probing atmospheric effects using GRAPES-3 plastic scintillator detectors

GRAPES-3 Collaboration

M. Zuberi^{1,a}, S. Ahmad², M. Chakraborty¹, A. Chandra², S. R. Dugad¹, U. D. Goswami³, S. K. Gupta¹, B. Hariharan¹, Y. Hayashi⁴, P. Jagadeesan¹, A. Jain¹, P. Jain⁵, V. B. Jhansi⁶, S. Kawakami⁴, H. Kojima⁷, S. Mahapatra⁸, P. K. Mohanty¹, Y. Muraki⁹, P. K. Nayak¹, T. Nonaka¹⁰, A. Oshima⁷, D. Pattanaik^{1,8}, M. Rameez¹, K. Ramesh¹, L. V. Reddy¹, S. Shibata⁷, F. Varsi⁵

¹ Tata Institute of Fundamental Research, Homi Bhabha Road, Mumbai 400005, India

² Aligarh Muslim University, Aligarh 202002, India

³ Dibrugarh University, Dibrugarh 786004, India

⁴ Graduate School of Science, Osaka Metropolitan University, Sugimoto, Sumiyoshi, Osaka 558-8585, Japan

⁵ Indian Institute of Technology Kanpur, Kanpur 208016, India

⁶ Department of Physics, Khalifa University, Abu Dhabi 127788, United Arab Emirates

⁷ College of Engineering, Chubu University, Kasugai, Aichi 487-8501, Japan

⁸ Utkal University, Bhubaneswar 751004, India

⁹ Institute for Space-Earth Environmental Research, Nagoya University, Nagoya 464-8601, Japan

¹⁰ Institute for Cosmic Ray Research, Tokyo University, Kashiwa, Chiba 277-8582, Japan

Received: 18 September 2023 / Accepted: 8 February 2024 / Published online: 11 March 2024

© The Author(s) 2024

Abstract The GRAPES-3 extensive air shower (EAS) array has been designed to study cosmic rays from 10^{13} – 10^{16} eV. It employs 400 scintillator detectors spread across $25,000\text{ m}^2$, mainly of cone-type and fiber-type, each covering a 1 m^2 area. These detectors record EAS particle densities and arrival times, which are crucial for determining primary particle energy and direction. A decade (2013–2022) of EAS data is analyzed to investigate the dependence of particle densities on ambient temperature and atmospheric pressure. Notably, ambient temperature exhibits a delayed response, with a more pronounced delay in fiber-type detectors, while cone-type detectors exhibit a higher observed temperature coefficient. In contrast, atmospheric pressure instantly and uniformly affects both detector types, with Monte Carlo simulations backing the observed pressure coefficient. These findings established a reliable pressure coefficient for EAS within this distinctive energy range and contributed to the refinement of correction algorithms, ultimately improving particle density precision for more accurate shower parameter estimates.

1 Introduction

The Sun's influence on terrestrial atmospheric dynamics is paramount, driven by the interplay of Earth's solar radiation and orbital motion. The atmosphere directly impacts the ground-based studies of cosmic rays (CRs) with its ever-changing characteristics. The change in the atmospheric pressure and temperature can cause discernible variations in the CR flux observed by surface detectors. When primary CRs enter Earth's atmosphere, they initiate a cascade of interactions with atmospheric nuclei, resulting in extensive air showers (EAS) development. Since the atmospheric pressure reflects the vertical air column density above the ground, a rise (fall) in atmospheric pressure signifies an augmented (reduced) mass overburden, which introduces a notable influence, particularly on EAS initiated by low-energy primary CRs. The outcome manifests as a decrease (increase) in observed particle counts at the observational level. Consequently, variations in atmospheric pressure, left unaccounted for, can introduce significant errors in estimating cosmic ray flux and energy. Thus, a profound comprehension of atmospheric effects and careful implementation of necessary corrections are essential for precise scientific investigations.

The atmospheric circulation is significantly influenced by the daily cycle of solar radiation. Scientists have exten-

^a e-mail: meeran.zuberi@epj.org (Corresponding author)

sively studied the recurring patterns of atmospheric pressure. The atmospheric solar heating, combined with regional forcing like upward eddy conduction of thermal heat from the ground, generates internal gravity waves in the atmosphere with periods of mainly diurnal and semi-diurnal harmonics. These waves cause regular oscillations in the atmospheric pressure, temperature and pressure fields, generally termed ‘atmospheric tides’ [1–4]. For surface pressure fields, the amplitude of semi-diurnal variation is regularly distributed, which is ~ 1 hPa at near-equatorial regions and rapidly decreases as we move towards the poles.

In 1911, a year before the discovery of cosmic rays (CRs), researchers noticed a subtle link between natural ionization and atmospheric pressure in oceanic atmospheric electricity measurements [5]. This marked the first sign of atmospheric pressure influencing CRs. An earlier experiment on the Eiffel Tower (about 300 m above ground) showed a similar dependence, but the effect was too faint to explain explicitly [6]. Subsequent in-depth studies, including one revealing a 0.7% reduction in ionization counts per 1 mmHg increase in pressure, emphasized the enduring significance of atmospheric pressure in achieving precise measurements [7]. Numerous studies in the following years explored seasonal impacts on atmospheric muons and particle densities in extensive air showers [8–10].

In another study, the impact of atmospheric pressure on extensive air showers (EAS) was investigated at the Pic-du-Midi EAS array, positioned at 2.86 km above sea level. The study, focusing on EAS arrays with 5 m and 80 m inter-detector separations at energies around $\sim 10^{14}$ eV, revealed pressure coefficients of $(-0.75 \pm 0.01)\% \text{ hPa}^{-1}$ for the 5 m configuration and $(-0.76 \pm 0.02)\% \text{ hPa}^{-1}$ for the 80 m configuration [11, 12]. Subsequent investigations using neutron monitors at high latitudes demonstrated pressure sensitivity with coefficients such as $(-0.710 \pm 0.006)\% \text{ hPa}^{-1}$ for Murchison Bay and Uppsala, $(-0.725 \pm 0.005)\% \text{ hPa}^{-1}$ for Resolute, Churchill, and Ottawa, and $(-0.736 \pm 0.004)\% \text{ hPa}^{-1}$ for locations like Mawson and Mt. Wellington. Discrepancies in coefficients were attributed to differences between neutron monitors and barometers rather than statistical variations [13]. In a recent study employing gamma rays in the 2–10 MeV range, an average pressure coefficient of $-0.4\% \text{ hPa}^{-1}$ was deduced, with differences from earlier studies attributed to the differences in rigidity and altitudes [14]. The Pierre Auger Observatory pursued a comprehensive analysis of atmospheric effects on particle densities, utilizing surface detectors to investigate over 9.6×10^5 extensive air shower events with energies exceeding $\geq 10^{18}$ eV. This examination showcased a pressure variation’s impact on event rates, indicating a reduction of about $(-0.27 \pm 0.3)\% \text{ hPa}^{-1}$ [15]. A recent study by the HAWC collaboration similarly unveiled pressure coefficients for scalar data recorded by

photomultiplier tubes (PMTs), yielding a value of $-0.343\% \text{ hPa}^{-1}$ [16].

Additionally, the upper atmospheric temperature undergoes seasonal variations due to the Earth’s orbital motion around the Sun, leading to changes in atmospheric density. Consequently, there is a corresponding seasonal variation in muon intensity, closely linked to the atmospheric temperature. Various studies have investigated this phenomenon, utilizing data from high-energy muon flux measurements obtained by deep underground experiments like MINOS and IceCube [8, 17]. These studies have focused on examining the impact of varying upper atmospheric temperatures, consistently reporting a positive temperature coefficient. The GRAPES-3 experiment has also explored the relationship between muon flux and upper atmospheric temperature using the GRAPES-3 muon telescope, specifically designed to detect low-energy (> 1 GeV) directional muon flux. A smaller negative dependence for atmospheric muons $(0.17 \pm 0.02)\% \text{ K}^{-1}$ has been observed compared to MINOS, which exhibited a high positive dependence $(0.873 \pm 0.009 \text{ (stats)} \pm 0.010 \text{ (syst)})$ [18]. This difference primarily stems from the higher energies of the muon flux recorded by MINOS (> 0.73 TeV) in comparison to the GRAPES-3 muon flux, which operates at approximately GeV energies. It’s worth mentioning that the upper-temperature variations above the MINOS detector are ~ 10 K, attributable to its high-latitude location. In contrast, the temperature variation for the GRAPES-3 location remains ~ 1 K throughout the year. Although this slight change may have some impact on the Molière radius of the EAS, as demonstrated by the other experiment [15]. Nevertheless, in the current investigation of high energy EAS, the predominant influence is the instrumental effect of local temperature. This factor poses a challenge in distinguishing the subtle effects resulting from variations in upper atmosphere temperature, and addressing this aspect falls beyond the scope of present study.

Situated near the equator, the GRAPES-3 experiment (Gamma Ray Astronomy at PeV Energies—phase 3) experiences a daily variation in atmospheric pressure of approximately one hPa that can lead to noticeable variations in the recorded CRs within the energy range of 10^{13} – 10^{16} eV. This work is possibly the first systematic investigation that examines how local temperature and atmospheric pressure influence CR measurements in this energy range, utilizing two distinct types of plastic scintillator detectors employed in the GRAPES-3 experiment. To validate the consistency of the observed pressure coefficient, we compared these findings with Monte Carlo simulation studies conducted earlier for this experiment [19]. This comparison underscores the robustness of the pressure coefficient values obtained through empirical measurements.

2 The GRAPES-3 experiment

The GRAPES-3 experiment, situated at an altitude of 2200 m above mean sea level in Ooty, India (11.4° N, 76.7° E), has been designed to examine the energy spectrum, nuclear mass composition and anisotropy of cosmic rays in the range of 10^{13} – 10^{16} eV [20–23]. Moreover, the experiment provides a unique potential to study solar, atmospheric, and thunderstorm phenomena [24–32]. The array is composed of two primary elements: (i) 400 plastic scintillator detectors, each covering an area of 1 m^2 , distributed across $25,000\text{ m}^2$ [26], and (ii) a large area tracking muon telescope with an area of 560 m^2 having an energy threshold of $\sec(\theta)$ GeV for muons arriving at an angle θ [27,28]. The arrangement of detectors in the GRAPES-3 EAS array follows a symmetric hexagonal geometry, with a mere 8 m of separation between neighbouring detectors. This design results in one of the most tightly packed configurations among conventional array types. This array consists of two types of plastic scintillator detectors namely cone-type and fiber-type. These detectors are unique in their distinct configurations. Both types consist of four blocks of plastic scintillators, each measuring $50 \times 50\text{ cm}^2$. However, the cone-type detectors possess a thickness of 5 cm, while the fiber-type detectors have a thickness of 2 cm. For cone-type detectors, the arrangement involves positioning the scintillator blocks within a square shape aluminum tank, as illustrated in Fig. 1. On top of a trapezoidal-shaped aluminum cone, a PMT with a diameter of 5 cm (model ETL9807B) is affixed, its face situated at a height of 60 cm above the scintillator surface. To enhance the effectiveness of collecting diffuse photons at the PMT, the interior surfaces of the tank and the cone are coated with super-white (TiO_2) paint. An additional sizable aluminium cover is used to safeguard the entire detector assembly from rain and the heating effects of direct sunlight.

In fiber-type detectors, photon collection is done using Kuraray's double-clad wavelength shifting (WLS) fibers of type Y11 (200). Two variations exist within the fiber-type detector category namely the single-PMT and dual-PMT fiber detectors. While the single-PMT fiber detector resembles the dual-PMT detector, it functions with just one high-gain PMT. The side-view of a complete dual-PMT WLS fiber detector is presented in Fig. 2.

In this configuration, photons originating from each $50 \times 50\text{ cm}^2$ scintillator tile are acquired by 18 fibers designated for the high-gain PMT, whereas 6 fibers are allocated for the low-gain PMT. These sets of 18 and 6 fibers, respectively designed for high- and low-gain PMTs, are accommodated within 12 grooves and subsequently linked to two PMTs through separate cookies. The first cookie comprises $18 \times 4 = 72$ fibers, responsible for the high-gain PMT, while

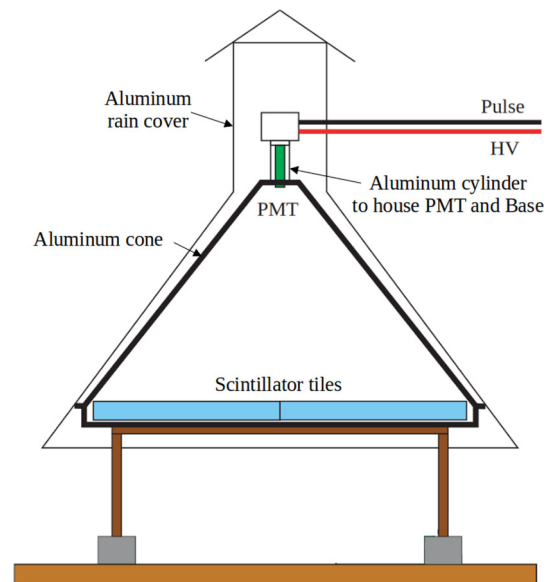


Fig. 1 Schematic of Cone-type scintillator detector. In this configuration, photons are directly captured by the PMT positioned atop the scintillator blocks at a height of 60 cm

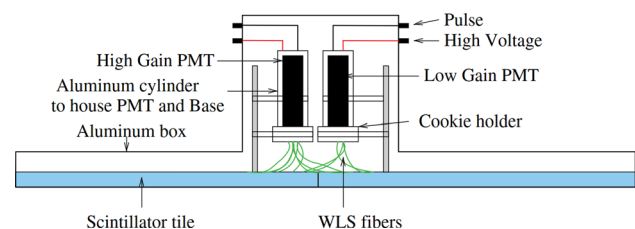


Fig. 2 Schematic of Fiber-type scintillator detector. In this configuration, photon collection is achieved by employing WLS fibers grooved over the scintillator blocks to improve photon collection efficiency

the second one holds $6 \times 4 = 24$ fibers directed to the low-gain PMT. To safeguard against external electrical interference, the PMT is enclosed within an aluminum cylinder. Vertically positioned at the core of an aluminum tank measuring $112 \times 103 \times 5\text{ cm}^3$, the two PMTs are encompassed. Afterwards, the entire assembly of scintillator and WLS fibers is wrapped in the two layers of Tyvek paper, functioning as a proficient yet diffusive reflector, significantly augments the collected photon quantity. Further elaboration on the performance analysis and simulation of the fiber-type detector can be found in other references [29,30].

The dissimilarities in geometry, photon collection techniques, and thermal insulation characteristics of these two types of scintillator detectors motivated us to conduct individual investigations of their responses to ambient temperature and atmospheric pressure, which will be described in the following sections.

3 Data preparation

The ten years of EAS data (1 January 2013 to 31 December 2022) of both the cone-type and fiber-type detectors have been utilized to investigate the influence of atmospheric effects on particle density. From 1 January 2013 to 8 September 2016, the GRAPES-3 EAS rate was ~ 35 Hz. Subsequently, it experienced an increase to ~ 50 Hz following an upgrade in the EAS trigger area, which was expanded from 14,000 to 19,000 m². At the GRAPES-3 location, the surface temperature and atmospheric pressure (hereafter named temperature and pressure, respectively) are measured every minute. The temperature was measured using *Davis Instruments* manufactured weather station (VANTAGE PRO-2), located at the EAS array centre, with a resolution of 0.1 °C. Two independent digital barometers were placed nearby to record pressure data, offering accuracy down to 0.1 hPa. Although occasional power interruptions or instrument issues could result in data gaps, two barometers and the rapid pressure equalization across a substantial area allowed us to employ a self-consistent approach to merge both pressure datasets and generate a continuous data stream of atmospheric pressure. The details of this method can be found elsewhere [31].

Issues within the scintillator detectors, associated electronics, or data recording systems can introduce instrumental artefacts and gaps into the data. We devised an algorithm to identify and eliminate these problematic periods to mitigate this. Initially, we computed the hourly particle densities for all plastic scintillator detectors by summing up the particles passing through them. Next, we applied a 24-h moving average, effectively acting as a low-pass filter to remove variations in the data of less than one day. We calculated the percentage deviation of the hourly rate with respect to the moving average value at that point. These values were then averaged over a day, effectively attenuating variations occurring on a daily timescale. A Gaussian function was then used to fit the distribution of daily averaged values for an entire period, and the standard deviation was determined. Any data point surpassing the ± 5 standard deviations threshold was flagged as bad, excluding that day from our analysis. On average, this process resulted in removing about 19% of data out of the total 3652 days, with these exclusions being randomly distributed among all plastic scintillator detectors. The missing data intervals are filled using the constant value of the last available data point for the application of the Fast Fourier Transform (FFT) technique. Nevertheless, for the analysis of temperature/pressure dependence, these particular data periods are excluded from all datasets. Out of the total available detectors, a subset of 178 cone-type and 169 fiber-type detectors were used in this study. Figure 3a shows the hourly variation of the averaged particle densities from

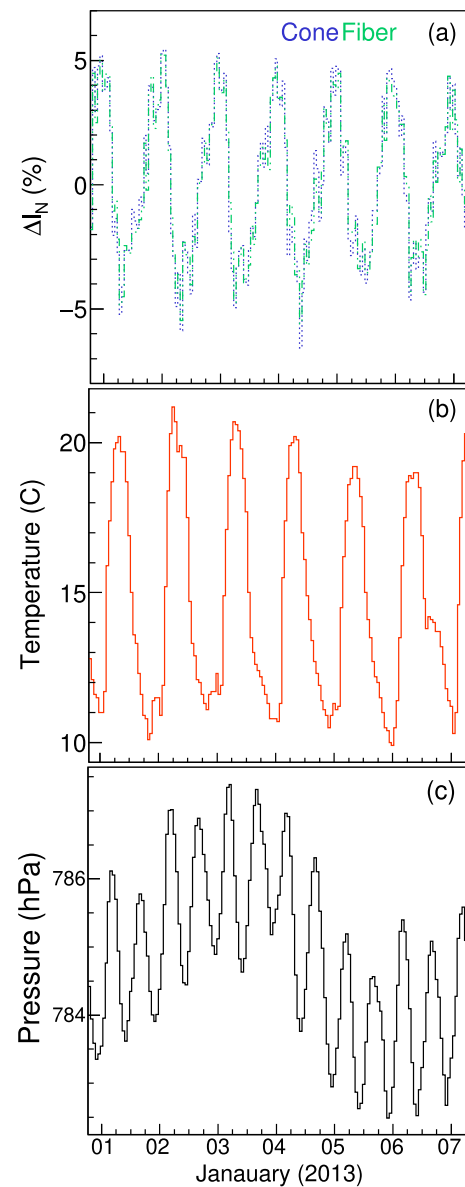


Fig. 3 Hourly variation of **a** averaged particle densities from cone-type (represented by dashed line) and fiber-type (represented by dotted line) detectors, **b** temperature, and **c** pressure data from 1 Jan 2013 to 7 Jan 2013. The particle densities in both cone-type and fiber-type detectors exhibit a prevailing 24-h periodic variation, aligning with the 24-h periodic variation observed in temperature in panels **a** and **b** respectively. Meanwhile, Ooty's pressure data indicates a predominant 12-h periodic variation, as depicted in panel **c**

cone and fiber type detectors ΔI_N as a percentage from 1 January 2013 to 7 January 2013, exhibiting daily variations.

4 Ambient temperature effect

In Ooty, the temperature data displays a prominent 24-h periodicity, while the pressure data exhibits a dominant 12-h peri-

odicity as displayed in Fig. 3b, c, respectively. We employed the FFT technique to individually analyse the dependencies on particle density. This algorithm utilizes the discrete Fourier transform to convert time-domain data into the frequency domain efficiently and vice versa. The frequency spectra for averaged particle densities of cone and fiber type detectors, temperature, and pressure obtained through FFT are shown in Fig. 4. In cone-type and fiber-type detectors, the dominant peak is observed at a 1 cycle per day (CPD) frequency with amplitudes of 1.6 and 1.5%, respectively. Similarly, the temperature frequency spectrum also displays a predominant peak at 1 CPD, with an amplitude of 2.4 °C due to its dominant 24-h periodic variations. The second most prominent peak in particle densities for cone- and fiber-type detectors is detected at 2 CPD, with amplitudes of 0.5 and 0.6%, respectively. This coincides with the dominant periodicity observed in atmospheric pressure, which has an amplitude of 1 hPa, as illustrated in panel (d) of Fig. 4.

To examine the temperature's effect on particle densities, we initially designed a narrow-band filter to select frequencies centred at $f_c = 1$ CPD having the 100% acceptance in the frequency range of 0.999 CPD to 1.001 CPD, and after that, it smoothly decreased to zero, as discussed in details elsewhere [32]. Subsequently, an Inverse Fast Fourier Transform (IFFT) was applied to the filtered frequency spectra for reverting it to the time domain. Our analysis revealed a distinct inverse relationship between particle densities obtained from scintillator detectors (cone- and fiber-type) and ambient temperature. However, the variations in particle densities exhibit a temporal offset compared to the temperature profile. This time offset was determined by shifting the temperature data forward and backwards by ± 8 h in 1-h increments relative to the particle densities. For each shift, we calculated the Pearson correlation coefficient (r). The time offset was estimated by fitting the cross-correlation distribution using a fifth-order polynomial function of order five. Panels (a) and (b) of Fig. 5 depict the cross-correlation plots for one fiber-type detector (det. 001) and one cone-type detector (det. 004), respectively. We identified a time offset of approximately 81 min with $r = -0.97$ for det. 001 and 52 min offset with $r = -0.98$ for det. 004.

Similarly, the time offset is computed for every cone-type and fiber-type detector. The average observed time offset is determined to be (53.7 ± 2.5) min for cone-type detectors and (70.9 ± 2.0) min for fiber-type detectors, as illustrated in Fig. 6. Notably, the time offset is greater in fiber-type detectors than in cone-type detectors.

After applying the time offset corrections in all the detectors, we determine the temperature dependence using Eq. (1).

$$\Delta I_N = \beta_T \cdot \Delta T \quad (1)$$

where, ΔI_N represents the normalized deviation of uncorrected particle densities, ΔT denotes the time offset corrected

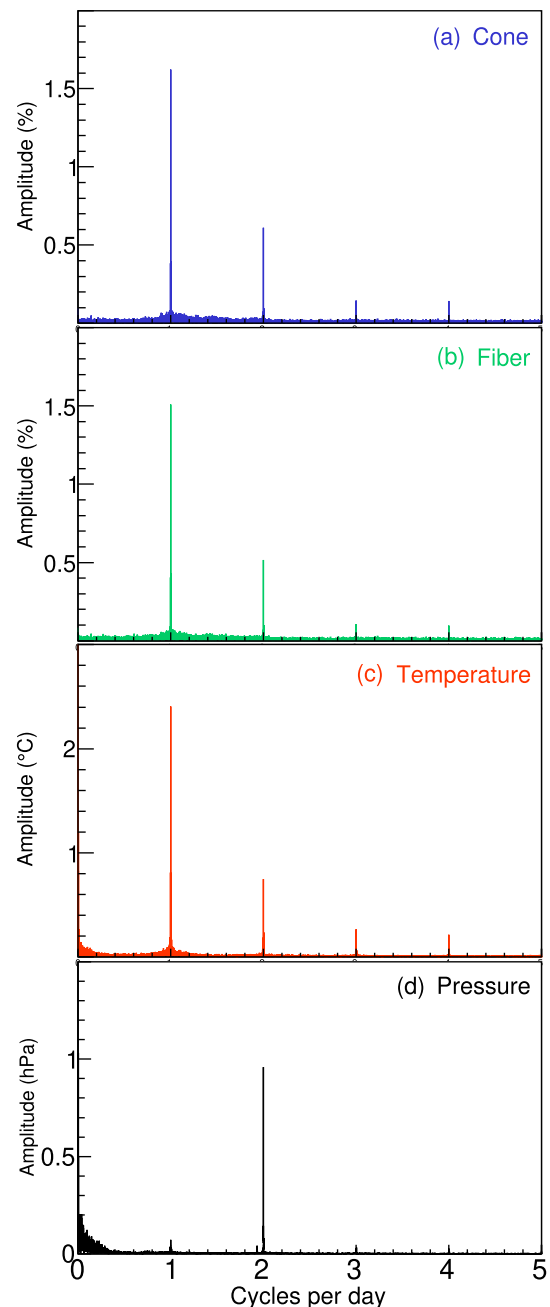


Fig. 4 Frequency spectrum obtained through FFT for **a** particle densities of cone-type, **b** particle densities of fiber-type, **c** temperature, and **d** pressure data for the period of 2013 to 2022

temperature deviation from its average, and β_T signifies the temperature coefficient. A least-squares fitting method has been used to determine the β_T value for all plastic scintillator detectors.

Figure 7 displays the distributions of β_T for cone-type and fiber-type detectors. These distributions exhibit mean values of $(-0.63 \pm 0.02)\% \text{ } ^\circ\text{C}^{-1}$ and $(-0.56 \pm 0.01)\% \text{ } ^\circ\text{C}^{-1}$, respectively. In contrast to the time offset, it is notable that the average β_T value is greater in the cone-type detectors

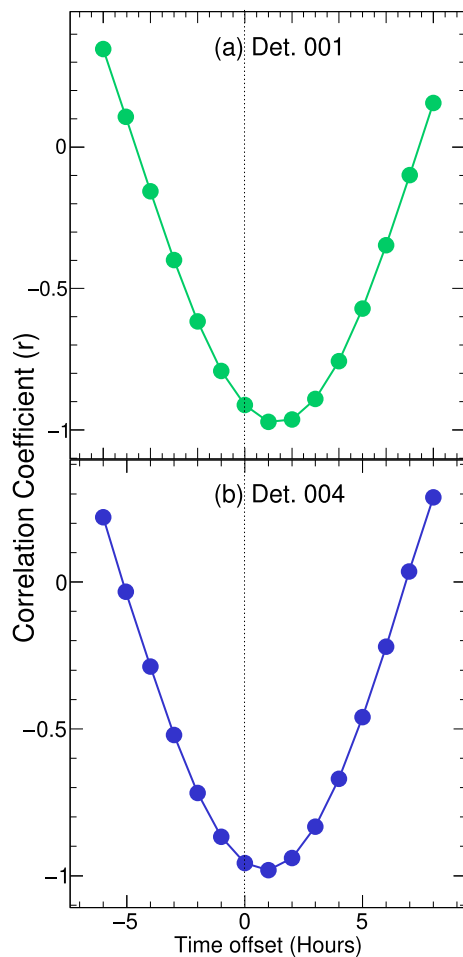


Fig. 5 Cross-correlation plots for a **a** fiber-type (det.001), and a **b** cone-type (det.004) detector. The vertical dotted line represents the zero time offset. The polynomial fit yields the time offset of 81 minute at -0.97 r-value and 52 minute at -0.98 r-value for det.001 and det.004 respectively

compared to the fiber-type detectors. However, due to large rms of the time offset and β_T distributions, we have opted to use the individual temperature coefficients of each detector to correct their particle densities for temperature-induced variations.

5 Atmospheric pressure effect

As previously explained, the atmospheric pressure in Ooty exhibits semi-diurnal variations, giving rise to the dominant peak at 2 CPD in the frequency spectrum, as depicted in Fig. 4d. In a manner analogous to what was done for calculating the temperature dependence, a similar approach was adopted for assessing the pressure dependence, as discussed previously in the context of β_T .

After applying the temperature corrections to the uncorrected particle densities, a narrow band filter was employed to

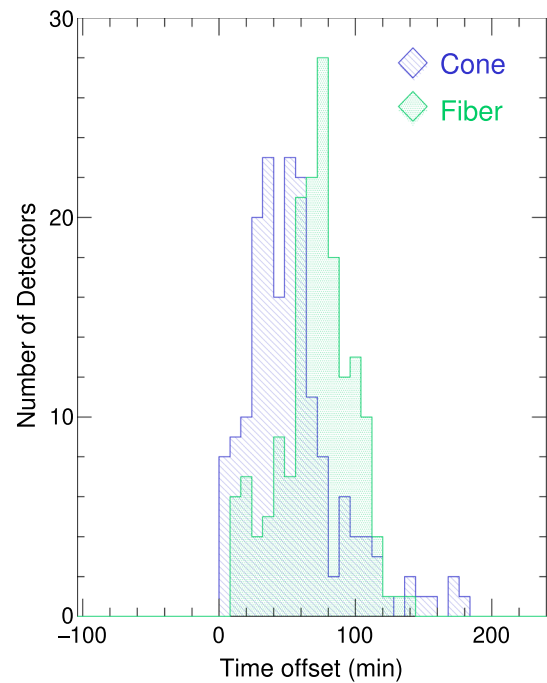


Fig. 6 Time offset distributions for cone-type (represented by line-filled histogram) and fiber-type (represented by dot-filled histogram) detectors. The average observed time offset is determined to be (53.7 ± 2.5) min for cone-type detectors and (70.9 ± 2.0) min for fiber-type detectors

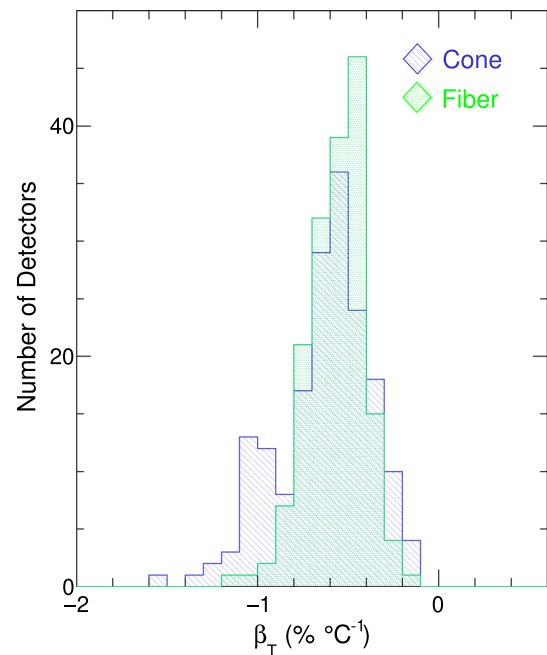


Fig. 7 β_T distributions for cone-type (represented by line-filled histogram) and fiber-type (represented by dot-filled histogram) detectors. The average β_T is determined to be $(-0.63 \pm 0.02)\% \text{ } ^\circ\text{C}^{-1}$ for cone-type detectors and $(-0.56 \pm 0.01)\% \text{ } ^\circ\text{C}^{-1}$ for fiber-type detectors

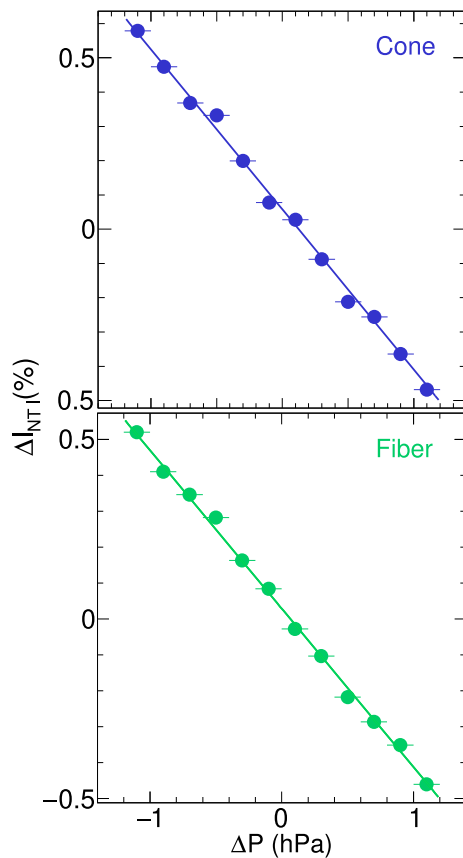


Fig. 8 Temperature corrected particle density change as a function of pressure for cone-type (top panel) and fiber-type (bottom panel) detectors. The β_P is determined to be $(-0.46 \pm 0.01)\% \text{ hPa}^{-1}$ for cone-type detectors and $(-0.44 \pm 0.01)\% \text{ hPa}^{-1}$ for fiber-type detectors

isolate frequencies centred at $f_c = 2$ CPD having 100% acceptance in the frequency range of 1.999 CPD to 2.001 CPD for temperature-corrected particle densities and the atmospheric pressure datasets. These filtered frequency components were then transformed into the time domain using IFFT. However, unlike the temperature effect, which is localized and anticipates varying dependencies in different detectors, the pressure effect arises from variations in atmospheric masses. It is expected to manifest similar effects across all detectors, regardless of their types, and should not exhibit any time offsets. To validate this hypothesis, we combined the data from all cone-type and fiber-type detectors and calculated the individual detector-type pressure coefficient (β_P) using Eq. (2).

$$\Delta I_{NT} = \beta_P \cdot \Delta P \quad (2)$$

where, ΔI_{NT} symbolizes the normalized deviation of temperature-corrected particle densities, while ΔP represents the deviation of pressure from its mean, and β_P denotes the pressure coefficient. We have employed a least-squares fitting approach to ascertain the β_P value for both

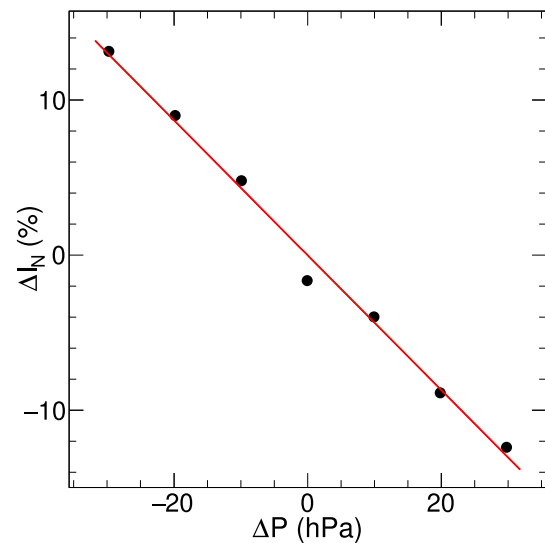


Fig. 9 Simulated particle density change as a function of pressure. The simulated β_P is determined to be $(-0.43 \pm 0.01)\% \text{ hPa}^{-1}$

cone-type and fiber-type detectors as shown in Fig. 8. The β_P value for cone-type detectors has been calculated as $(-0.46 \pm 0.01)\% \text{ hPa}^{-1}$, while for fiber-type detectors, it stands at $(-0.44 \pm 0.01)\% \text{ hPa}^{-1}$. Remarkably, these values are practically identical within the margins of error.

6 Monte Carlo simulation

The equatorial climate is characterized by consistently high temperatures throughout the year, primarily due to the direct and consistent incidence of sunlight. This condition generally results in a relatively stable atmosphere in these regions. In Ooty, the diurnal pressure variation remains within a narrow range of approximately one hPa throughout the entire year. Since pressure indicates the vertical density of the atmosphere above the surface, any changes in atmospheric density are reflected in pressure, subsequently influencing CR flux. To investigate this phenomenon, we conducted simulations involving 35×10^4 proton-initiated EASs within the energy spectrum ranging from 10^{13} – 10^{16} eV, covering the angular domain of 0° – 60° for zenith angles and 0° – 360° for azimuth angles using the CORSIKA-v76900 package [33]. These simulations incorporated a combination of high-energy (SIBYLL [34]) and low-energy (FLUKA [35]) hadronic interaction models.

The density of the four lower layers exhibits an exponential relationship with altitude, which can be mathematically expressed in terms of the atmospheric mass thickness overburden, denoted as $M(h)$, and the height h , utilizing Eq. (3)

$$M(h) = a_i + b_i \cdot e^{-h/c_i} \quad (3)$$

where, ‘i’ runs from layers 1 to 4. However, for the 5th layer, the mass overburden decreases linearly with height and follows the Eq. (4).

$$T(h) = a_5 - b_5 \cdot h/c_5 \quad (4)$$

Here, a, b and c are the parameters taken from the “Central European atmosphere for June 16, 1993” (ATMOD5) atmospheric model. This model offers the most closely matching atmospheric density value of $\sim 803 \text{ g}\cdot\text{cm}^{-2}$ at the altitude of Ooty, where the observed density is $800 \text{ g}\cdot\text{cm}^{-2}$. Subsequently, the parameter b was adjusted by varying its value by $\pm 15\%$ in steps of 5%. The simulated showers were randomly thrown ten times over the GRAPES-3 fiducial area after including the detector response using GEANT4 [36]. We then computed the total number of particles observed in all detectors. Figure 9 illustrates the percentage change in the observed total number of particles for different pressure values. The linear fit yields the value of simulated β_P is $(-0.43 \pm 0.01)\% \text{ hPa}^{-1}$. Moreover, the resilience of the observed results is verified by incorporating an alternative atmospheric profile, specifically the “US standard atmosphere” parameterized by Linsley (ATMOD1). Similar to the approach with the ATMOD5 atmospheric model, the strategy for determining β_P is applied in the case of ATMOD1. The result for the SIBYLL-FLUKA model combination is determined to be $(-0.42 \pm 0.01)\% \text{ hPa}^{-1}$, exhibiting consistency with ATMOD5 within the margin of errors. Additional information regarding this simulation and the outcomes associated with various combinations of high- and low-energy interaction models can be found elsewhere [19].

7 Discussion

The high statistical EAS data recorded by the cone- and fiber-type plastic scintillator detectors of the GRAPES-3 experiment made it possible to explore precisely how ambient temperature and atmospheric pressure influence particle density. An initial visual examination of each detector’s time series particle density data over the entire data collection period hinted at a repeating pattern, seemingly on a 24-h cycle. However, the frequency spectra of the observed particle density not only confirmed the presence of the expected 24-h periodicity but also unveiled a distinct 12-h periodicity.

As previously discussed, the plastic scintillator detectors in the GRAPES-3 experiment employ PMTs to convert photons from scintillator detectors into signals. These PMTs feature photocathodes composed of bialkali material, specifically Be-Cu, with a temperature sensitivity specified by the manufacturer at $-0.5\% \text{ }^\circ\text{C}^{-1}$ [37]. In a previous study, a temperature coefficient of $-0.5\% \text{ }^\circ\text{C}^{-1}$ for PMTs is reported, and it is proposed that this coefficient may arise from fluctuations in the Fermi level and cathode resistance.

Additionally, it is noted that these coefficients vary not only between different types of PMTs but also among PMTs made from similar materials [38].

Ooty maintains a relatively consistent yearly average temperature of around $\sim 15 \text{ }^\circ\text{C}$, a characteristic that remains stable across the years. However, outside temperature shows significant variations from day to night, particularly during winter (November to February), where temperatures can vary by approximately $\pm 10 \text{ }^\circ\text{C}$. All detectors are deployed in an open area, exposing them to these drastic environmental temperature changes. These observations suggest that the 24-h fluctuations in particle density primarily stem from the sensitivity of the PMTs to external temperature changes. While there might be some contribution from the temperature sensitivity of the plastic scintillators, it is noteworthy that organic scintillator light output remains essentially unaffected by temperature within a range of -60 to $20 \text{ }^\circ\text{C}$, as suggested by previous study [38]. The observed mean temperature dependence for cone-type detectors is found to be higher, quantified at $(0.63 \pm 0.02)\% \text{ }^\circ\text{C}^{-1}$, compared to fiber-type detectors, which exhibit a value of $(-0.56 \pm 0.01)\% \text{ }^\circ\text{C}^{-1}$, which is possibly due to the better insulation of fiber-type detectors than cone-type.

Another interesting outcome of the study reveals that particle densities in all scintillator detectors do not exhibit an immediate response to external temperature variations. Instead, they display a pronounced anti-correlation with temperature after a certain delay, determined to be $(53.7 \pm 2.5) \text{ min}$ for cone-type and $(70.9 \pm 2.0) \text{ min}$ for fiber-type detectors.

As previously mentioned, the scintillator detectors are enclosed within an aluminum tank, with an additional aluminum rain cover placed above them for protection during adverse weather conditions. Consequently, any temperature gradient resulting from external temperature shifts needs time to propagate through these detector covers, the inside air column, and an aluminum case of PMT before reaching the photocathode. Moreover, the temperature measurements are from a single location, while the scintillator detectors are distributed across a substantial area spanning $25,000 \text{ m}^2$. This spatial disparity leads to slight differences between the recorded and actual temperatures at each detector location. The combination of these factors collectively contributes to the observed time offset in the responses of the scintillator detectors to temperature changes. The increased delay observed in fiber-type detectors compared to cone-type detectors can be attributed to their superior insulation due to the presence of larger air columns between the external aluminum cover and the PMT aluminum casing. This insulation results in a slower response to changes in the external temperature gradient, thereby protecting the detector’s PMT over a more extended period. This hypothesis has been independently verified by constructing a basic three-layer toy model

for both types of detectors, where the air column is assumed to be sandwiched between two aluminum layers. Notably, the thermal resistance is observed to be 26% lower in cone-type detectors compared to fiber-type detectors, which could potentially explain the 29% lesser average time-delay values in cone-type detectors. The details of the model have been comprehensively explained in the Appendix A. It is important to note that these values provide a rough understanding of the primary reason for the delay, and for precise calculations, a more complex model is required.

It is well-established that the cosmic ray intensities detected by surface detectors are subjected to the influence of atmospheric pressure. The atmospheric pressure directly reflects the vertical air mass above the measurement location. High-pressure conditions indicate a greater atmospheric mass, reducing the mean free path of secondary cosmic rays and increasing their interactions within the atmosphere. Consequently, lower-energy cosmic rays are more likely to be absorbed within the atmosphere, decreasing the observed shower rate at the surface and vice versa. The variations in atmospheric pressure at equatorial regions exhibit a dominant 12-h component. These variations were measured at approximately one hPa at the GRAPES-3 site during the analysis period, as illustrated in Fig. 4d. Therefore, as previously explained, a second dominant peak in the particle density spectra can be attributed to the influence of atmospheric pressure. The mean pressure dependence for both cone-type and fiber-type detectors was determined to be highly comparable, with values of $(-0.46 \pm 0.01)\% \text{ hPa}^{-1}$ for cone-type detectors and $(-0.44 \pm 0.01)\% \text{ hPa}^{-1}$ for fiber-type detectors. Additionally, there was no observable lag between particle density and pressure. This absence of lag was anticipated since the pressure effect is unrelated to detector characteristics.

In a previously published investigation [19], an extensive Monte Carlo simulation was conducted. This simulation involved the adjustment of atmospheric parameters within the CORSIKA package, coupled with the utilization of the GEANT4 response for all plastic scintillator detectors. The simulated pressure coefficient was determined by employing a combination of the SIBYLL-FLUKA interaction models for low and high energy interactions and is found to be $(-0.43 \pm 0.01)\% \text{ hPa}^{-1}$. Remarkably, this value aligns closely with the mean observed values obtained for both cone-type and fiber-type detectors, underscoring the reliability and consistency of our findings.

8 Conclusion

The GRAPES-3 experiment, using cone- and fiber-type plastic scintillator detectors, provides valuable insights into how ambient temperature and atmospheric pressure affect

the cosmic rays within the energy range of 10^{13} – 10^{16} eV. Despite an overall stable average, temperature variations at the experimental site affect detectors due to the significant role of temperature sensitivity of PMTs. Notably, particle density exhibits an anti-correlation with temperature, with discernible delays attributed to detector enclosures and spatial temperature variations. The smaller temperature dependence and enhanced delay in fiber-type detectors are due to superior insulation, safeguarding PMTs. The pressure dependence of cosmic rays has also been reported, exhibiting a consistent mean pressure dependence across different detector types, and is well supported by Monte Carlo simulations. These findings will also prove valuable for implementing correction algorithms for observed particle densities, ultimately enhancing the accuracy of shower parameter estimations.

Acknowledgements We thank D.B. Arjunan, A.S. Bosco, V. Jeyakumar, S. Kingston, N.K. Lokre, K. Manjunath, S. Murugapandian, S. Pandurangan, B. Rajesh, R. Ravi, V. Santoshkumar, S. Sathiyaraj, M.S. Shareef, C. Shobana, R. Sureshkumar, P.S. Rakshe and B.S. Rao for their role in the efficient running of the experiment. We acknowledge the support of the Department of Atomic Energy, Government of India, under Project Identification No. RTI4002. Grants from Chubu University and ICRR of Tokyo University, Japan, partially supported this work. We thank the anonymous referee whose extensive and incisive comments led to a considerable improvement of the paper.

Data Availability Statement This manuscript has no associated data or the data will not be deposited. [Authors' comment: The raw datasets analyzed during the current study are available to all the GRAPES-3 collaboration members and maybe available to others on reasonable request.]

Code Availability Statement The manuscript has no associated code/software. [Author's comment: The code/software developed during the current study are available to all the GRAPES-3 collaboration members.]

Open Access This article is licensed under a Creative Commons Attribution 4.0 International License, which permits use, sharing, adaptation, distribution and reproduction in any medium or format, as long as you give appropriate credit to the original author(s) and the source, provide a link to the Creative Commons licence, and indicate if changes were made. The images or other third party material in this article are included in the article's Creative Commons licence, unless indicated otherwise in a credit line to the material. If material is not included in the article's Creative Commons licence and your intended use is not permitted by statutory regulation or exceeds the permitted use, you will need to obtain permission directly from the copyright holder. To view a copy of this licence, visit <http://creativecommons.org/licenses/by/4.0/>.
Funded by SCOAP³.

Appendix A: Toy-model for heat transfer dynamics

While creating a thermal model that precisely replicates the thermal insulation in both types of detectors necessitates intricate simulations involving the exact geometry and thermal properties of each detector component, we have, for a

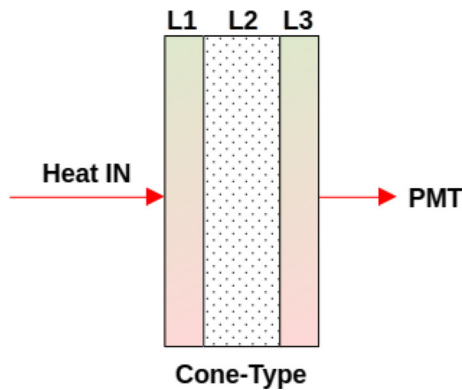


Fig. 10 Simplified model for cone-type detector. Here, layers L1 and L3, composed of aluminum having a thickness of 0.3 mm, and layer L2 is the air column, assumed to be 10 cm

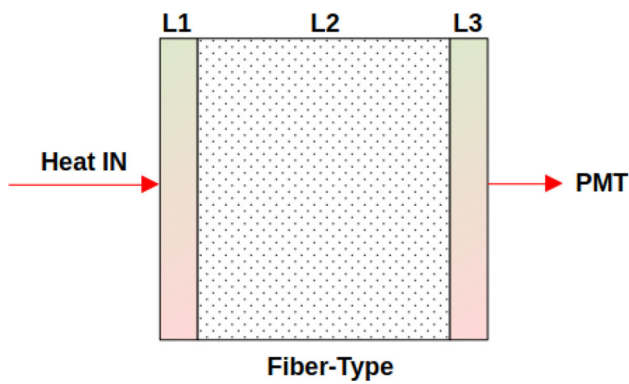


Fig. 11 Simplified model for fiber-type detector. Here, layers L1 and L3, composed of aluminum having a thickness of 0.3 mm, and layer L2 is the air column, assumed to be 45 cm

basic comparison and analytical calculation of heat transfer coefficient and thermal resistance, devised a simplified model for both detector types. In terms of geometry, heat must traverse approximately three layers-L1, L2, and L3, as illustrated in Figs. 10 and 11 in Appendix A.

Layers L1 and L3, composed of aluminum with a thermal conductivity of $237 \text{ W}/(\text{m} \cdot \text{K})$, are common to both types of detectors, each with a length of 3 mm. However, the presence of air (thermal conductivity $= 0.026 \text{ W}/(\text{m} \cdot \text{K})$) volume in L2, between these two layers, significantly influences thermal insulation. We have taken an approximate area of 1 m^2 for the Fiber-type detector and, due to the PMT's location at the neck part of the detector, we have reduced the area by 70% for the cone-type detector, resulting in 0.3 m^2 . The length of L2 is assumed to be 10 and 45 cm in cone-type and fiber-type detectors, respectively. The heat transfer coefficient can be defined as:

$$\frac{1}{U_t} = \frac{1}{A} \sum_{i=1}^n \frac{L_i}{k_i}$$

where U_t is the heat transfer coefficient, A is the contact area, L is the thickness of the n^{th} layer, and k is the thermal conductivity of layer material. The calculated total heat transfer coefficient is $0.078 \text{ W}/(\text{m}^2 \cdot \text{K})$ for the cone-type detector and $0.058 \text{ W}/(\text{m}^2 \cdot \text{K})$ for the fiber-type detectors. Additionally, thermal resistances have been calculated, equivalent to the reciprocal of the heat transfer coefficient, resulting in values of $12.8^\circ\text{C}/\text{W}$ for cone-type detectors and $17.3^\circ\text{C}/\text{W}$ for fiber-type detectors.

References

1. R.S. Lindzen, S. Chapman, Atmospheric tides. *Space Sci. Rev.* **10**, 3–188 (1969). <https://doi.org/10.1007/s11207-012-0078-6>
2. B. Haurwitz, A.D. Cowley, The diurnal and semidiurnal barometric oscillations global distribution and annual variation. *PAGEOPH* **102**, 193–222 (1973). <https://doi.org/10.1007/BF00876607>
3. H.H. Hsu, B.J. Hoskins, Tidal fluctuations as seen in ECMWF data. *Q. J. R. Meteorol. Soc.* **115**, 247–264 (1989). <https://doi.org/10.1002/qj.49711548603>
4. A. Dai, J. Wang, Diurnal and semidiurnal tides in global surface pressure fields. *J. Atmos. Sci.* **56**, 3874–3891 (1999). [https://doi.org/10.1175/1520-0469\(1999\)056<3874:DASTIG>2.0.CO;2](https://doi.org/10.1175/1520-0469(1999)056<3874:DASTIG>2.0.CO;2)
5. G.C. Simpson, C.S. Wright, Atmospheric electricity over the ocean. *Proc. R. Soc. Lond.* **A85**, 175–199 (1911). <https://doi.org/10.1098/rspa.1911.0031>
6. A. De Angelis, Spontaneous ionization to subatomic physics: Victor Hess to Peter Higgs. *Nucl. Phys. B Proc. Suppl.* **243–244**, 3–11 (2013). <https://doi.org/10.1016/j.nuclphysbps.2013.09.008>
7. L. Myssowsky, L. Tuwim, Unregelmäßige Intensitätsschwankungen der Höhenstrahlung in geringer Seehöhe. *Zeitschrift für Physik* **39**, 146–150 (1926). <https://doi.org/10.1007/BF01321981>
8. P. Adamson et al. (MINOS Collaboration), Observation of muon intensity variations by season with the MINOS far detector. *Phys. Rev. D* **81**, 012001 (2010). <https://doi.org/10.1103/PhysRevD.81.012001>
9. M. Ambrosio et al. (MACRO Collaboration), Seasonal variations in the underground muon intensity as seen by MACRO. *Astropart. Phys.* **7**, 109 (1997). [https://doi.org/10.1016/S0927-6505\(97\)00011-X](https://doi.org/10.1016/S0927-6505(97)00011-X)
10. M.D. Berkova et al., Temperature effect of the muon component and practical questions for considering it in real time. *Bull. Russ. Acad. Sci. Phys.* **75**, 820–824 (2011). <https://doi.org/10.3103/S1062873811060086>
11. A. Daudin, J. Daudin, Effets atmospheriques sur les gerbes d'Auger. *J. Atmos. Terrest. Phys.* **3**, 245 (1953). [https://doi.org/10.1016/0021-9169\(53\)90124-X](https://doi.org/10.1016/0021-9169(53)90124-X)
12. L.I. Dorman, Cosmic rays in the earth's atmosphere and underground. Kluwer Academic Publishers, Dordrecht (2004). https://link.springer.com/book/10.1007/978-1-4020-2113-8?utm_medium=referral&utm_source=google_books&utm_campaign=3_pier05_buy_print&utm_content=en_08082017
13. S. Lindgren, On the pressure dependence of the cosmic ray intensity recorded by the standard neutron monitor. *Tellus* **14**, 44 (1962). <https://doi.org/10.1111/j.2153-3490.1962.tb00118.x>
14. G. Datar et al., Barometric pressure correction to gamma-ray observations and its energy dependence. *JCAP* **09**, 045 (2021). <https://doi.org/10.1088/1475-7516/2021/09/045>
15. J. Abraham et al. (Pierre Auger observatory Collaboration), Atmospheric effects on extensive air showers observed with the surface detector of the Pierre Auger observatory. *Astropart. Phys.*

- 32(2), 89–99 (2009). <https://doi.org/10.1016/j.astropartphys.2009.06.004>
16. K.P. Arunbabu et al. (HAWC collaboration), Atmospheric pressure dependence of HAWC scaler system, PoS ICRC2019, 1095 (2019). <https://doi.org/10.22323/1.358.1095>
17. T. Gaisser et al. (IceCube Collaboration), Seasonal Variation of Atmospheric Muons in IceCube, PoS ICRC2019, 894 (2019). <https://doi.org/10.22323/1.358.0894>
18. K.P. Arunbabu et al., (GRAPES-3 collaboration), Dependence of the muon intensity on the atmospheric temperature measured by the GRAPES-3 experiment. *Astropart. Phys.* **94**, 22 (2017). <https://doi.org/10.1016/j.astropartphys.2017.07.002>
19. M. Zuberi et al. (GRAPES-3 Collaboration), Simulation of atmospheric pressure dependence on GRAPES-3 particle density. *Exp. Astron.* **49**, 61–71 (2020). <https://doi.org/10.1007/s10686-020-09653-0>
20. F. Varsi et al. (GRAPES-3 Collaboration), Cosmic ray energy spectrum and composition measurements from the GRAPES-3 experiment: latest results. PoS ICRC2021, 388 (2021). <https://doi.org/10.22323/1.395.0388>
21. M. Chakraborty et al. (GRAPES-3 Collaboration), Large-scale cosmic ray anisotropy measured by the GRAPES-3 experiment. PoS ICRC2021, 393 (2021). <https://doi.org/10.22323/1.395.0393>
22. D. Pattanaik et al. (GRAPES-3 Collaboration), Validating the improved angular resolution of the GRAPES-3 air shower array by observing the Moon shadow in cosmic rays. *Phys. Rev. D* **106**, 022009 (2022). <https://doi.org/10.1103/PhysRevD.106.022009>
23. B. Hariharan et al. (GRAPES-3 Collaboration), Energy sensitivity of the GRAPES-3 EAS array for primary cosmic ray protons. *Exp. Astron.* **50**, 185–198 (2020). <https://doi.org/10.1007/s10686-020-09671-y>
24. P.K. Mohanty et al. (GRAPES-3 Collaboration), Transient Weakening of Earth's Magnetic Shield Probed by a Cosmic Ray Burst. *Phys. Rev. Lett.* **117**, 171101 (2016). <https://doi.org/10.1103/PhysRevLett.117.171101>
25. B. Hariharan et al. (GRAPES-3 Collaboration), Measurement of the electrical properties of a thundercloud through muon imaging by the GRAPES-3 experiment. *Phys. Rev. Lett.* **122**, 105101 (2019). <https://doi.org/10.1103/PhysRevLett.122.105101>
26. S.K. Gupta et al. (GRAPES-3 Collaboration), GRAPES-3-A high-density air shower array for studies on the structure in the cosmic-ray energy spectrum near the knee. *NIM* **540**, 311–323 (2005). <https://doi.org/10.1016/j.nima.2004.11.025>
27. Y. Hayashi et al. (GRAPES-3 Collaboration), A large area muon tracking detector for ultra-high energy cosmic ray astrophysics-the GRAPES-3 experiment. *NIM* **545**, 643–657 (2005). <https://doi.org/10.1016/j.nima.2005.02.020>
28. F. Varsi et al. (GRAPES-3 Collaboration), A GEANT4 based simulation framework for the large area muon telescope of the GRAPES-3 experiment. *JINST* **18**, P03046 (2023). <https://doi.org/10.1088/1748-0221/18/03/P03046>
29. P.K. Mohanty et al. (GRAPES-3 Collaboration), Measurement of some EAS properties using new scintillator detectors developed for the GRAPES-3 experiment. *Astropart. Phys.* **31**, 24 (2008). <https://doi.org/10.1016/j.astropartphys.2008.11.004>
30. P.K. Mohanty et al. (GRAPES-3 Collaboration), Monte Carlo code G3sim for simulation of plastic scintillator detectors with wavelength shifter fiber readout. *Rev. Sci. Instrum.* **83**, 043301 (2012). <https://doi.org/10.1063/1.3698089>
31. P.K. Mohanty et al. (GRAPES-3 Collaboration), Solar diurnal anisotropy measured using muons in GRAPES-3 experiment in 2006. *Pramana* **81**, 343–357 (2013). <https://doi.org/10.1007/s12043-013-0561-0>
32. P.K. Mohanty et al. (GRAPES-3 Collaboration), Fast Fourier transform to measure pressure coefficient of muons in the GRAPES-3 experiment. *Astropart. Phys.* **79**, 23–30 (2016). <https://doi.org/10.1016/j.astropartphys.2016.02.006>
33. D. Heck et al., CORSIKA: a Monte Carlo code to simulate extensive air showers. FZKA-6019 (1998). <https://inspirehep.net/literature/469835>
34. J. Engel et al., Nucleus–nucleus collisions and interpretation of cosmic-ray cascades. *Phys. Rev. D* **46**, 5013 (1992). <https://doi.org/10.1103/PhysRevD.46.5013>
35. F. Cerutti et al., Nuclear model developments in FLUKA for present and future applications. EPJ Web Conf. **146**, 12005 (2017). <https://doi.org/10.1051/epjconf/201714612005>
36. J. Allison et al., Recent developments in Geant4. *Nucl. Instrum. Methods Phys. Res. A* **835**, 186–225 (2016). <https://doi.org/10.1016/j.nima.2016.06.125>
37. E.T. Enterprises, ET photomultipliers products. <https://et-enterprises.com/products/photomultipliers>
38. W.R. Leo, *Techniques for nuclear and particle physics experiments* (Springer, Berlin, 1994). <https://doi.org/10.1007/978-3-642-57920-2>